

Nanostructured manganese oxide and manganese oxide/polyethylenedioxythiophene rods electrodeposited onto nickel foam for supercapacitor applications

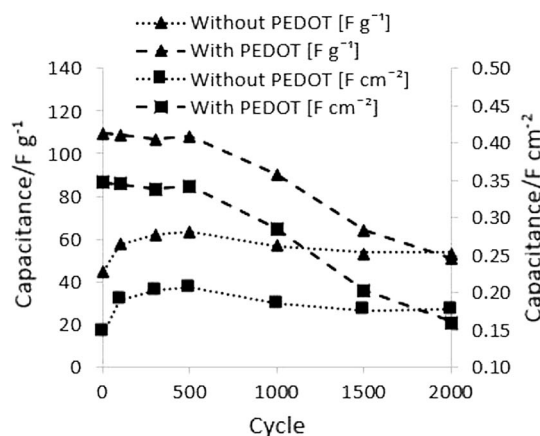
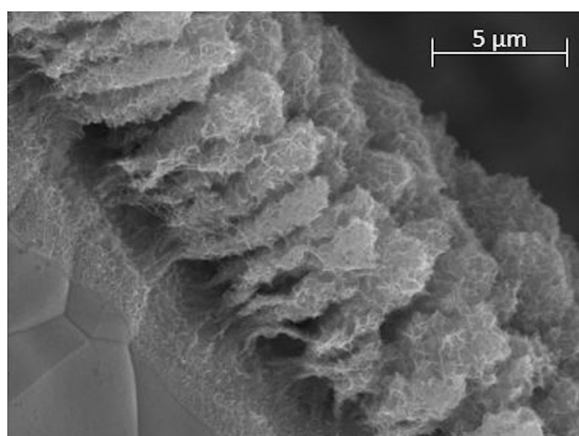
Michael P. Clark¹ · Wei Qu² · Douglas G. Ivey¹

Received: 8 July 2016 / Accepted: 3 October 2016 / Published online: 12 October 2016
© Springer Science+Business Media Dordrecht 2016

Abstract A template-free anodic electrodeposition process was utilized to deposit Mn oxide and Mn oxide/PEDOT rods onto Ni foam substrates for use as supercapacitor electrodes. Deposit morphology was optimized by varying deposition conditions and by characterization using electron microscopy. The deposits were poorly crystalline, and electron diffraction patterns could be indexed to either a cubic spinel structure (Mn_3O_4) or a hexagonal birnessite structure (MnO_2). The deposits had an overall oxidation state of Mn^{3+} before cycling and Mn^{4+} after 500 cycles. The maximum capacitance values for deposits with and

without PEDOT were 159 and 120 F g^{-1} (500 and 290 mF cm^{-2}), respectively, measured using CV at a scan rate of 5 mV s^{-1} . The addition of the PEDOT coating reduced Mn oxide dissolution during cycling up to 500 cycles. Uncoated samples showed an increase in capacitance during cycling, which is attributed to the oxidation state change and the redeposition of Mn oxide in areas of high conductivity. Capacitance retentions after 2000 cycles were 46 and 120 % for deposits with and without PEDOT, respectively.

Graphical Abstract



✉ Douglas G. Ivey
doug.ivey@ualberta.ca

¹ Department of Chemical and Materials Engineering,
University of Alberta, Edmonton, AB T6G 2V4, Canada

² National Research Council—Energy, Mining and
Environment, Vancouver, BC V6T 1W5, Canada

Keywords Manganese oxide · PEDOT · Nickel foam ·
Electrodeposition · Supercapacitors

1 Introduction

The increasing emphasis on renewable energy sources, driven by the move away from fossil fuels, has sparked growing interest in energy storage. Electrochemical supercapacitors (ES) are candidates for energy storage because of their high power densities and long cycle lives. These devices bridge the power/energy gap between batteries and conventional capacitors. Applications include hybrid and electric vehicles, portable electronics, and renewable energy grids [1–4].

Depending on their dominant charge storage mechanism, ES can be classified into two groups: electrical double layer capacitors (EDLC) and Faradaic capacitors. EDLC store charge through the accumulation of ions at an electrode surface, while Faradaic capacitors store charge through reversible redox reactions in the bulk as well as at the surface of the electrode. For both charge storage mechanisms, the capacitance of an electrode is highly dependent on its surface area [1, 4].

Many materials exhibit supercapacitance, including transition metal oxides [5–9], carbon materials [10–14], and conducting polymers [15–17]. Of these materials, Mn oxide is of particular interest because it is environmentally benign, inexpensive, and has a large theoretical capacitance (1100–1300 F g⁻¹). Charge storage in Mn oxide is mostly Faradaic, with some contribution from the electrochemical double layer. Because of Mn oxide's poor electronic and ionic conductivity, it is difficult to achieve the theoretical capacitance while maintaining a reasonable level of mass loading. Another challenge for Mn oxide is dissolution during cycling. There are multiple ways of addressing the dissolution problem, including application of a protective coating or by modifying the electrolyte. [3, 4] Being a transition metal, Mn forms oxides in a variety of stable compositions and crystal structures. The electrochemical properties of Mn oxide are dependent on its atomic and crystal structure, as well as a number of other factors including morphology, porosity, and defect chemistry. By altering these structural parameters, it is possible to modify and optimize the electrochemical properties of a Mn oxide deposit [4, 5].

For the development of Mn oxide ES, the capacitance of a device can be improved by tailoring the Mn oxide in two ways. The first method is to improve the specific capacitance [F g⁻¹] of the Mn oxide, i.e., to improve the utilization of each gram of material deposited. This can be achieved in a number of ways, such as increasing the surface area or improving the conductivity of the deposit. The second way to improve the capacitance of a device is to increase the amount of material deposited, also known as mass loading (g cm⁻²). By increasing the amount of active

material on the substrate, more charge can be stored, resulting in improved areal capacitance (F cm⁻²). However, increasing the mass loading will usually result in morphology changes that degrade the specific capacitance; there is typically a tradeoff between mass loading and specific capacitance. This is largely because of Mn oxide's poor electronic and ionic conductivities; thicker deposits are highly resistive, which reduce electron and ion access to parts of the deposit.

As described in previous work [18–21], our group has developed a template-free anodic electrodeposition process to deposit high surface area, rod-like Mn oxide onto Au-coated Si. This template-free process allows for easy production of high surface area Mn oxide deposits compared with template-assisted methods, such as those using anodic alumina oxide, which can be quite complex and are impractical for large-scale applications [5, 18]. Electropolymerization of 3,4-ethylenedioxythiophene (EDOT) was used to coat the deposits with the conductive polymer, polyethylenedioxythiophene (PEDOT). The PEDOT coating improved capacitance from 185 to 285 F g⁻¹ and also improved capacitance retention after 250 cycles from 75 to 92 %. This increase in performance was attributed to the PEDOT shell providing an interconnected network that facilitated charge-transfer and electron conduction, and reduced dissolution during cycling. [19] The purpose of this paper is to reproduce this rod-like Mn oxide/PEDOT structure on Ni foam, with the aim of improving the mass loading and, subsequently, areal capacitance. Nickel foam was selected as the substrate because it is inexpensive, conductive, and its porosity should facilitate high degrees of mass loading.

Several studies in the literature have focused on achieving high areal capacitance on planar surfaces with Mn oxide and Mn oxide composites, and these typically achieve values around 100–300 mF cm⁻² [22–24]. Manganese oxide and Mn oxide composites prepared using high surface area substrates such as Ni foam have capacitances ranging from 100 to 2790 mF cm⁻² with most values in the range of 500–1000 mF cm⁻² [25–28].

2 Experimental

2.1 Mn oxide deposition

All electrodepositions were performed on Ni foam disks, which were 1.8 cm in diameter. The disks were ultrasonically cleaned in acetone and then ethanol for 10 min each. Depositions were performed using a modified cell and modified electrolyte, relative to the one used in our previous work [18, 19, 21]. The electrodes were horizontal,

instead of vertical, which provided better deposit uniformity. A schematic of the cell configuration is shown in Fig. 1. Electrolyte was flushed through the Ni foam before deposition to remove trapped air in the porosity of the foam. Samples were rotated at 75–200 rpm at a distance of 1 cm away from the Pt mesh counter electrode. Manganese oxide was anodically electrodeposited onto the Ni foam disks using a solution of 0.01 M $\text{Mn}(\text{C}_2\text{H}_3\text{O}_2)_2$ (Mn acetate), 0.02 M $\text{NH}_4(\text{C}_2\text{H}_3\text{O}_2)$ (ammonium acetate), and 10 % $\text{C}_2\text{H}_6\text{OS}$ (dimethyl sulfoxide (DMSO)). Depositions were performed at 60 °C for 2.5–10 min with a current density of 5–25 mA cm^{-2} . Current density was calculated using the geometric area of the Ni foam. The initial deposition conditions were taken from our previous work, as these conditions resulted in well-defined rod structures on Au-coated Si [18–21]. The deposition conditions were then varied to apply the deposition process to Ni foam. After deposition, the samples were rinsed in deionized water, dried in air at 100 °C for 60 min, and then stored in a vacuum desiccator. The mass of the deposits was measured using a Mettler-Toledo UMX2 ultra-microbalance with an accuracy of 0.1 μg .

2.2 PEDOT deposition

PEDOT was deposited through electropolymerization using a three electrode set up, with a saturated calomel electrode (SCE) as the reference electrode and Pt mesh as the counter electrode. The working electrode was the electrodeposited Mn oxide on Ni foam. The counter and working electrodes were placed vertically 2 cm apart. The electrolyte consisted of 0.08 M EDOT, 0.2 M LiF_4B , and

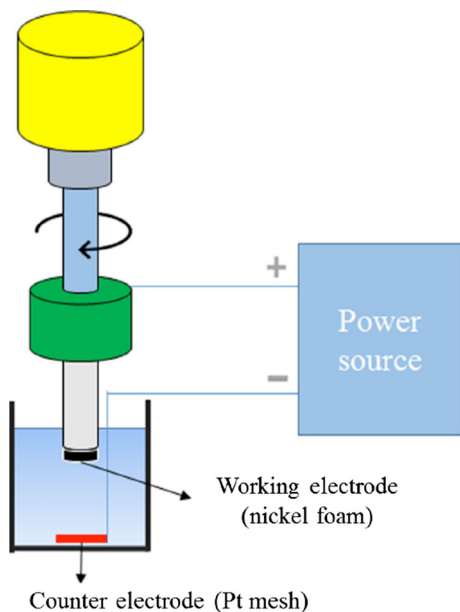


Fig. 1 Cell schematic for Mn oxide deposition on Ni foam

0.14 M sodium dodecyl sulfate. It was important to use a freshly prepared electrolyte, as solutions older than 24 h produce poor quality deposits. Electropolymerization was performed at a constant potential of 1 V vs. SCE for 45 s at 25 °C. The conditions and solution composition used for electropolymerization of PEDOT were taken from our previous work, as these conditions provided the best improvement to capacitive performance [19].

2.3 Electrochemical characterization

Electrochemical testing was performed using a Biologic SP-300 potentiostat. All electrochemical tests were conducted using an electrolyte of 0.5 M Na_2SO_4 , with a Pt counter electrode and an SCE reference electrode; all reported potentials are with respect to SCE. Cyclic voltammetry (CV) was used to determine capacitive performance of Mn oxide deposits. All CV measurements were performed in the 0–0.9 V range. Extended cycling was performed using CV for up to 2000 cycles at a scan speed of 20 mV s^{-1} .

2.4 Microstructural characterization

Deposit morphology was characterized using two scanning electron microscopes (SEMs); a Tescan Vega-3 SEM and a Zeiss Sigma SEM. All imaging processes were performed using secondary electrons (SE). A Zeiss Orion He-ion microscope (HIM) was used for higher-resolution, surface-sensitive imaging.

Two field emission transmission electron microscopes (TEMs) were used for high-resolution imaging and crystallographic analysis. The two instruments used were a Phillips CM-20, equipped with an Oxford EDX detector and operated at 200 kV; and the other a Hitachi HF-3300, operated at 300 kV. To prepare samples for TEM analysis, deposits were scraped off the substrate and ultrasonically suspended in ethanol. One or two drops of the suspension were then placed on a C-coated Cu grid and allowed to dry.

The oxidation states of the elements in the Mn oxide deposits were determined using X-ray photoelectron spectroscopy (XPS) (Kratos AXIS Ultra spectrometer), with a monochromatic Al source. The system was operated at 210 W with a pass energy of 20 eV. XPS spectra were calibrated using the C 1 s peak located at a binding energy of 285 eV.

3 Results and discussion

3.1 Mn oxide deposition conditions

Using porous Ni foam as the substrate for electrodeposition introduced some challenges for obtaining reproducible and

uniform microstructures. Initial depositions, using a solution containing only $\text{Mn}(\text{C}_2\text{H}_3\text{O}_2)_2$, produced deposits with poor uniformity. Ammonium acetate ($\text{NH}_4(\text{C}_2\text{H}_3\text{O}_2)$) and DMSO were chosen as additives and greatly improved deposit uniformity and reproducibility. Ammonium acetate acts as a buffer, and DMSO improves the wettability between the substrate and electrolyte. All deposits reported in this work are fabricated from electrolytes containing 0.01 M Mn acetate, 0.02 M ammonium acetate, and 10 % DMSO.

Manganese oxide deposits were fabricated over a range of nominal current densities (based on the geometrical area), from 5 to 25 mA cm^{-2} for 2.5 min, in order to optimize the deposition conditions. Images of some sub-optimal deposits are shown in Fig. 2. Deposits prepared at current densities less than 20 mA cm^{-2} resulted in a thin uniform layer of Mn oxide across the surface (Fig. 2a). Deposits prepared at 25 mA cm^{-2} yielded fused Mn oxide rods (Fig. 2b), which suffered from delamination from the Ni surface. Well-defined and adhered rods were obtained at a current density of 20 mA cm^{-2} ; this is the current density chosen for all subsequent depositions for this study.

Using the cell configuration shown in Fig. 1, samples were rotated horizontally during deposition. By rotating the sample in a horizontal configuration, we were able to minimize the variation in agitation, improving the uniformity of the deposition. Deposits were prepared using rotation speeds from 50 to 100 rpm. The optimal speed was determined to be 75 rpm, which resulted in a uniform coating of free-standing Mn oxide rods. Deposits prepared at 50 rpm were nonuniform (Fig. 2c), and deposits prepared at 100 rpm were thick layers of fused Mn oxide rods (Fig. 2d).

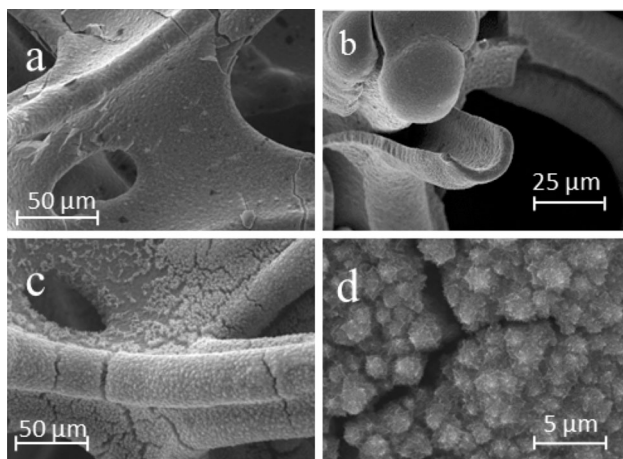


Fig. 2 SEM SE images of Mn oxide deposits prepared under suboptimal conditions: **a** 10 mA cm^{-2} , **b** 25 mA cm^{-2} , **c** 50 rpm, 20 mA cm^{-2} , **d** 100 rpm, 20 mA cm^{-2} . All deposits were prepared using 2.5 min as the deposition time

Samples were prepared at various deposition times in order to obtain different degrees of mass loading. The average masses of the deposited Mn oxide were 1.5, 3, and 5 mg cm^{-2} for deposition times of 2.5, 5, and 10 min, respectively. The microstructures of the deposits are shown in Fig. 3. For a deposition time of 2.5 min, the deposit consists of Mn oxide rods across the majority of the sample (Fig. 3a, d). The packing of the rods is not very tight, which means that a large portion of the Ni foam surface is not utilized. Increasing the deposition time to 5 min does not change the structure of individual rods drastically, but tighter packing of the rods occurs (Fig. 2b, e). Because of their similar structure, it is expected that the 2.5- and 5-min samples exhibit similar specific capacities. Cyclic voltammetry at 10 mV s^{-1} yields specific capacities of 133 and 130 F g^{-1} for the 2.5- and 5-min deposits, respectively. A deposition time of 10 min produces a deposit consisting of Mn oxide rods that have fused together to create a near continuous layer of Mn oxide (Fig. 2c, f). Because there is a volume change upon drying, this layer cracks and peels during drying. The specific capacitance for the 10-min deposit was 57 F g^{-1} at 10 mV s^{-1} . The drop in capacitance as the deposition time is increased from 5 to 10 min is attributed to the thickness of the deposit, the fusion of the rods preventing electrolyte access, and delamination of the deposit from the current collector. Although the 10-min sample had a higher mass loading than the 2.5- and 5-min samples, the detrimental changes to deposit morphology caused a substantial drop in specific capacitance, resulting in a drop in areal capacitance as deposition time was increased from 5 to 10 min. Deposits at 2.5, 5, and 10 min exhibited areal capacities of 220, 330, and 250 mF cm^{-2} , respectively. Because the 5-min sample exhibited the highest areal capacitance, 5 min was selected as the optimal deposition time.

For the optimal electrodeposition conditions, i.e., 5-min deposition time, 75 rpm rotation speed, and a current density of 20 mA cm^{-2} , the morphology consists of rod-shaped Mn oxide across most of the sample surface. Current efficiencies were estimated for electrodeposition. Accurate values could not be determined, because the exact oxide composition was not known due to the mixed valence of the deposited Mn oxide. However, the lowest efficiency was calculated as $\sim 42\%$ assuming Mn_3O_4 deposition ($\text{Mn}^{3+}/\text{Mn}^{2+}$) and close to 100 % for MnO_2 ; the actual efficiency is likely some value between the two. Trapped air bubbles during deposition create areas that allow for imaging of the rods from the side; one such area is shown in Fig. 4a. The rods are about 10 μm in length, tapered toward the substrate, and about 2 μm wide at their largest width. Edges of the Ni foam act as current risers, resulting in denser packing of rods in these areas. The rods themselves are very fibrous and are composed of many thin

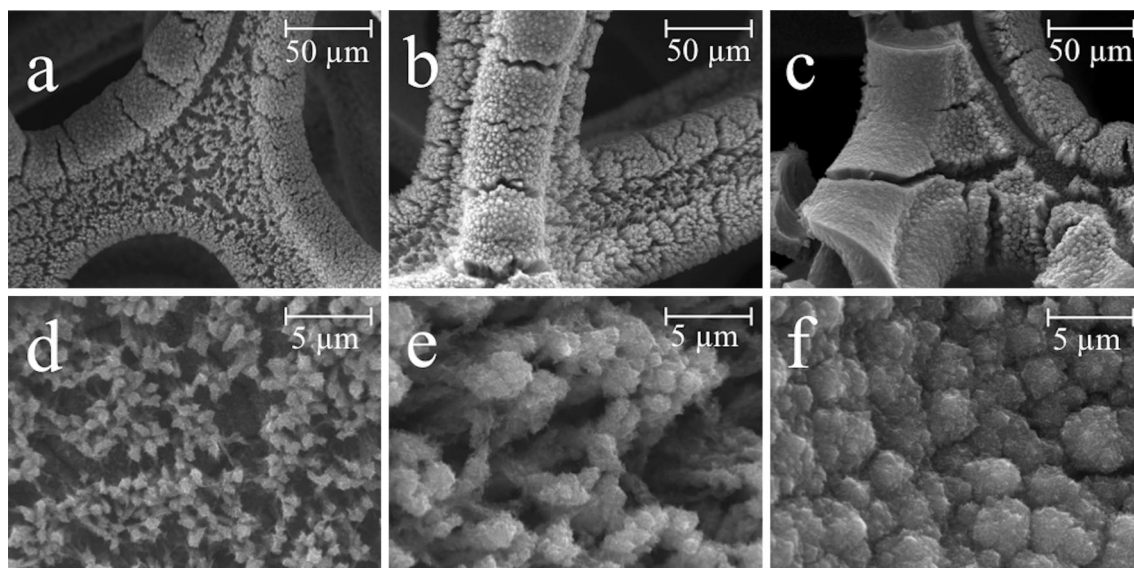


Fig. 3 SEM SE images of Mn oxide deposits prepared under varying deposition times: **a, d** 2.5 min, **b, e** 5 min, and **c, f** 10 min. Deposition current density was 20 mA cm^{-2} , and the rotation speed was 75 rpm

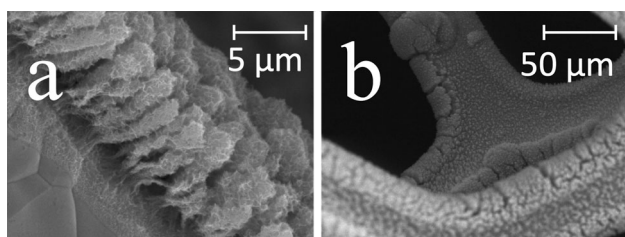


Fig. 4 SEM SE images of Mn oxide deposits: **a** Side view of Mn oxide rods, and **b** Mn oxide deposit within the Ni foam porosity. Deposition current density was 20 mA cm^{-2} , and the rotation speed was 75 rpm

sheets. The fibrous structure of the rods increases the surface area of the deposit, improving the capacitive performance. The surface area of the rods was measured in a recent publication by our group, using Brunauer–Emmett–Teller (BET) analysis; a value of $143 \text{ m}^2 \text{ g}^{-1}$ was obtained along with an average pore diameter of 13.5 nm. [20] Deposition of Mn oxide extends into the porosity of the Ni foam; e.g., see Fig. 4b. Manganese oxide has been observed to be deposited as deep into the foam as SEM imaging allows, which is about four layers deep. SEM imaging becomes more difficult in areas deep within the porosity. The morphology of the deposit within the Ni foam porosity varies from continuous coatings to well-defined rods. The porous structure of the Ni foam affects the agitation and effective current density that different areas of the Ni foam experience during deposition. These variations in conditions give rise to a variety of microstructures in areas deep within the porosity of the foam.

3.2 PEDOT deposition

Electropolymerization was utilized to produce coaxial core/shell Mn oxide/PEDOT rods on the Ni foam. At relatively low magnifications, there is no noticeable morphology difference between the two types of deposits (Fig. 5a–d). The presence of PEDOT was confirmed by EDX microanalysis in the SEM. The spectra (not shown here) from coated samples had a distinct S peak (from the EDOT), not present in uncoated samples. HIM was used to view the microstructures at much higher magnification and with improved surface sensitivity. The HIM images clearly show a difference in structures between the coated and uncoated samples; the thin sheet structure of the rods is clearly visible in the uncoated sample (Fig. 5e). The Mn oxide rods are conformally coated by porous PEDOT, with an apparent loss in surface area (Fig. 5f).

3.3 Transmission electron microscopy

TEM results for the as-deposited and cycled (500 cycles at 20 mV s^{-1}) Mn oxide deposits, prepared at 20 mA cm^{-2} and 75 rpm for 5 min, are shown in Fig. 6. Figure 6a shows a cluster of Mn oxide sheets from a single rod. A selected area electron diffraction (SAED) pattern was obtained from the area in Fig. 6a. The diffraction pattern shown in Fig. 6b consists of three weakly intense and diffuse rings, which indicate that the structure is poorly crystalline. There are different possible Mn oxides; however, the best indexing of the diffraction pattern was achieved for either the cubic spinel $\text{Fd-3m Mn}_3\text{O}_4$ structure or the hexagonal birnessite R-3m MnO_2 structure [29]. The

d spacings for the rings are 0.240, 0.209, and 0.140 nm, which, respectively, correspond to the (311), (400), and (440) planes of the cubic spinel structure. The 0.240 and 0.140 nm spacings also match, respectively, with the (006) and (119) planes of the hexagonal birnessite structure. The 0.209-nm ring matches with the birnessite diffraction data as well, but Miller indices were not assigned for that reflection [29]. A faint spot is present at a d spacing of 0.165 nm, which is consistent with the (511) plane of the cubic spinel structure and the (301) plane of the hexagonal birnessite structure. It should be noted that X-ray diffraction was also performed on these samples, but no significant peaks appeared because of the poor crystallinity.

The bright field image for the cycled deposit (Fig. 6c) shows a cluster of Mn oxide sheets, which are very similar to the as-deposited sample. The diffraction pattern (Fig. 6d) obtained from these sheets consists of three rings at d spacings of 0.241, 0.211, and 0.140 nm, which are very similar to the values for the as-deposited sample. The rings for the cycled sample are more defined, indicating better crystallinity. For the cycled sample, as with the as-deposited sample, the diffracted rings can be indexed to either the cubic spinel structure (Mn_3O_4) or the hexagonal birnessite

structure (MnO_2). There is evidence of preferred orientation of the Mn oxide deposit as well. The darkfield image in Fig. 6e, taken with part of the first two diffracted rings, shows many nanoscale grains of about 5 nm diameter.

High-resolution images of the as-deposited and cycled deposits are shown in Fig. 6f, g. Figure 6f (the as-deposited Mn oxide) was generated using a large enough objective aperture to include all three rings in Fig. 6b and shows Mn oxide sheets. The sheet in the center of the image is folded in such a way that allows part of the sheet to be viewed edge on. Using this image, the thickness of the sheet was determined to be about 3 nm. Other sheets are up to 5 nm in thickness. Lattice planes are observed on a few parts of the sheet, i.e., the crystalline portions, with a lattice spacing of about 0.52 nm. The observed lattice planes are likely the (111) planes of the cubic spinel structure or the (101) planes of the hexagonal birnessite structure; these planes have d spacings of 0.49 and 0.48 nm, respectively. Any differences in d spacings between the images and the diffraction database are likely due to distortion of the sheets.

Figure 6g shows a high-resolution image of a cycled deposit; this image was also generated by including all three rings, in Fig. 6d, in the objective aperture. Figure 6g shows a few agglomerated Mn oxide sheets, with one sheet viewed edge on. Along the length of this sheet, lattice planes are observed with a spacing of 0.56–0.61 nm which is relatively close to the (101) plane spacing for the hexagonal birnessite structure ($d = 0.48$ nm) and the (111) plane spacing for the cubic spinel structure ($d = 0.49$ nm). Lattice planes are also observed on a sheet oriented perpendicular to the beam direction. The spacings of these planes is in the range of 0.22–0.24 nm, which is consistent with the (006) plane ($d = 0.244$ nm) of the birnessite structure and two planes from the cubic spinel structure ((311) and (222) with spacings of 0.254 and 0.243 nm, respectively).

3.4 X-ray photoelectron spectroscopy

The Mn 3s XPS spectra for the as-deposited and cycled Mn oxide deposits, prepared at 20 mA cm^{-2} and 75 rpm for 5 min and then annealed at 100°C for 1 h, are shown in Fig. 7a. The cycled sample underwent 500 cycles at a scan rate of 20 mV s^{-1} . Peak splitting of the Mn 3s spectrum was used to determine the oxidation state of the Mn oxide deposits. Peak splitting was determined by fitting a pair of best-fit curves to the experimental data and measuring the peak-to-peak separation of the curves. The separation of the Mn 3s peak increases with decreasing Mn valence due to fewer unpaired electrons in the 3d orbital. Peak splitting data from Chigane et al. [30] and Gorlin and Jaramillo [31] have been compiled and are plotted in Fig. 7b. Figure 7b

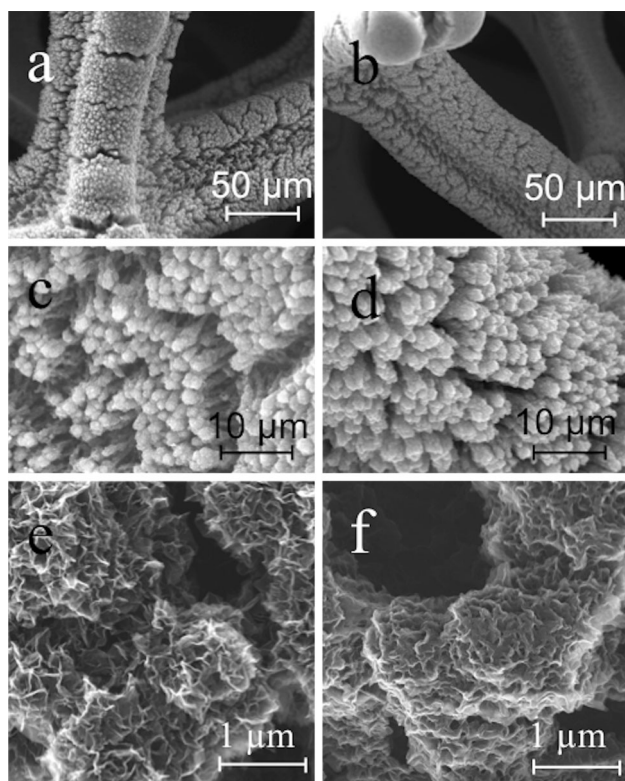


Fig. 5 SEM SE images of Mn oxide deposits: **a, c** without PEDOT; **b, d** with PEDOT. HIM SE images of Mn oxide deposits: **e** without PEDOT and **f** with PEDOT. Mn oxide deposits were prepared using 20 mA cm^{-2} for 5 min at 75 rpm. The PEDOT coating was prepared at 1 V for 45 s

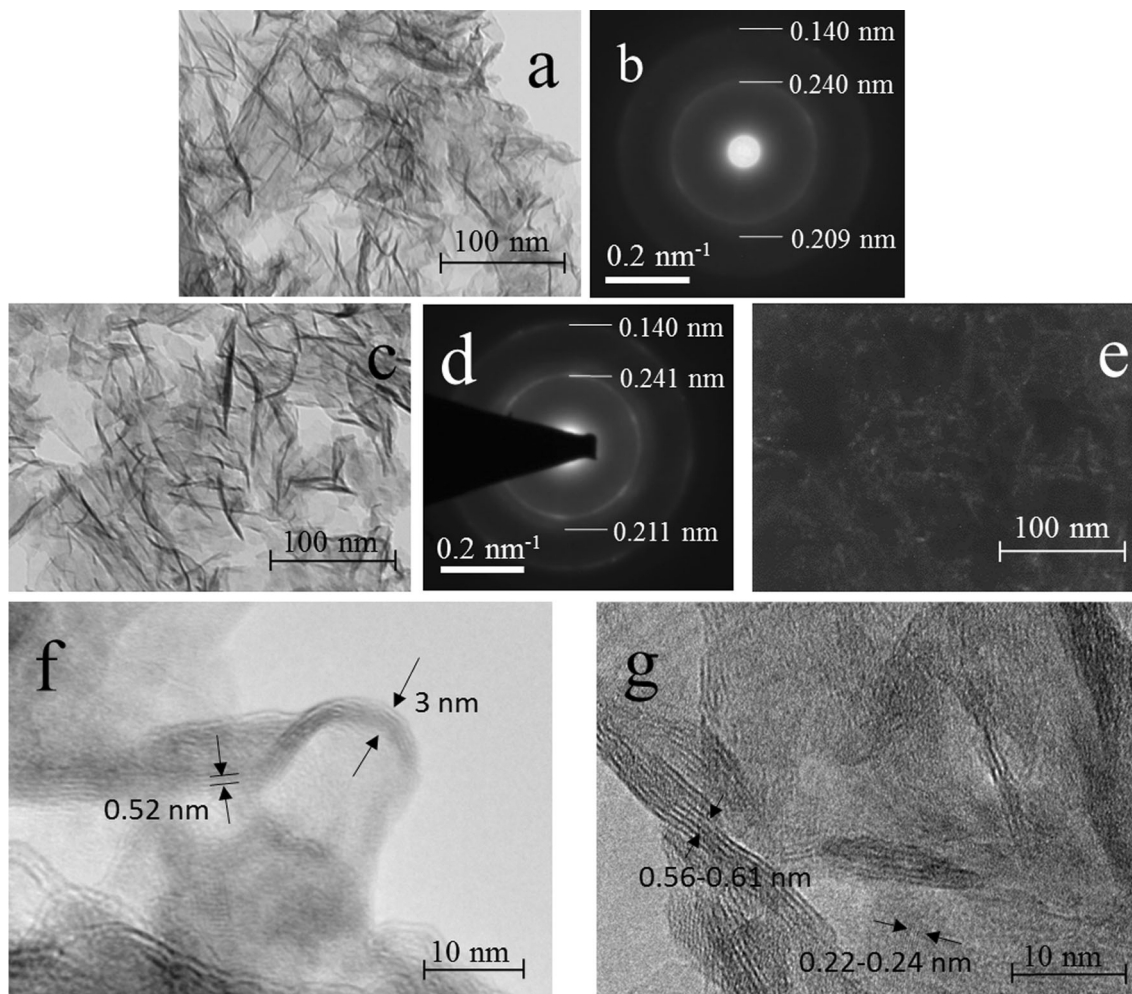


Fig. 6 TEM results for Mn oxide deposits. **a, b, f** The as-deposited; and **c–e, g** cycled 500 times at 20 mV s^{-1} . **a, c** Bright field images; **b, d** SAED patterns from the regions shown in **a** and **c**. **e** dark field image, and **f, g** high-resolution TEM images of the as-deposited **f** and cycled **g** samples at 20 mV s^{-1} for 500 cycles. The samples were

deposited at 20 mA cm^{-2} for 10 min, with a rotation speed of 75 rpm. The SAED patterns can be indexed to either a spinel or birnessite structure. Spinel: 0.209–0.211 nm (400); 0.240–0.241 nm (311); 0.140 nm (440). Birnessite: 0.209–0.211 nm (no indices in database [29]); 0.240–0.241 nm (006); 0.140 nm (119)

also shows the peak splitting measured from the as-deposited and cycled samples. The measured peak splitting for the as-deposited and 500 times cycled samples were 5.1 and 4.5 eV, respectively. Comparing these results with the plot in Fig. 7b shows that the cycled sample has an oxidation state of Mn^{4+} , and the as-deposited sample has an oxidation state of Mn^{3+} . With cycling, the Mn^{3+} present in the as-deposited sample is oxidized; after 500 cycles, the deposit is composed almost entirely of MnO_2 (Mn^{4+}). Combining the XPS results with the electron diffraction analysis above indicates that MnO_2 in the cycled sample is likely in the form of birnessite.

3.5 Cyclic voltammetry

Cyclic voltammetry results for Mn oxide and Mn oxide/PEDOT deposits are shown in Fig. 8. At scan speeds of 5

and 10 mV s^{-1} , anodic and cathodic waves are observed at around 0.5 and 0.35 V, respectively. These waves are caused by cation deintercalation during oxidation and cation insertion during reduction [25]. These waves disappear at larger scan rates because the intercalation/deintercalation kinetics are limited by Mn oxide's poor ionic conductivity.

The PEDOT coating provides a conductive pathway for electrons to access the poorly conductive Mn oxide. Manganese oxide has a conductivity of around 10^{-6} – $10^{-5} \text{ S cm}^{-1}$, while PEDOT has a conductivity on the order of 100 S cm^{-1} [32, 33]. The improved conduction of deposits with PEDOT yields higher capacitance, improved rate capability (up to 100 mV s^{-1}), and a voltammogram closer to the ideal rectangular shape. Maximum capacitance values were 159 F g^{-1} (500 mF cm^{-2}) and 120 F g^{-1} (290 mF cm^{-2}) at 5 mV s^{-1} with and without PEDOT,

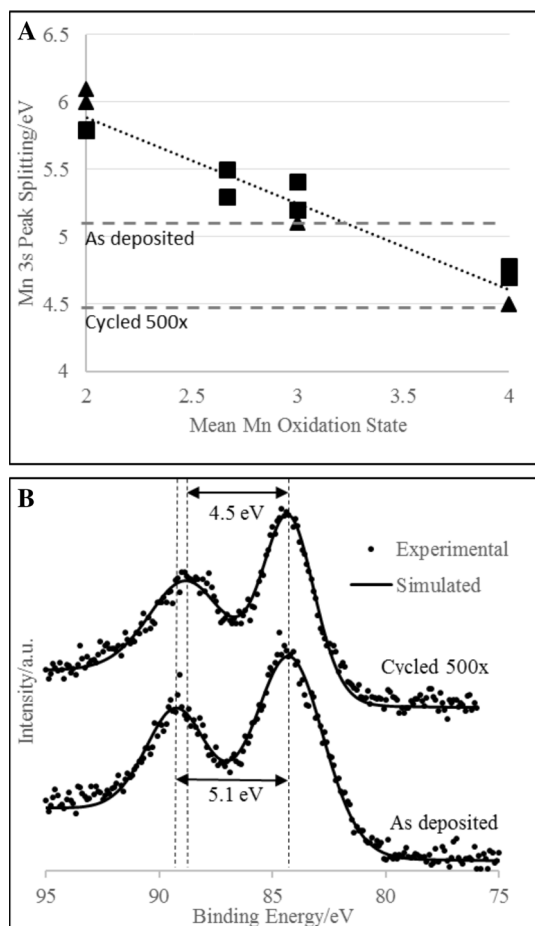


Fig. 7 **a** XPS Mn 3s spectra for the as-deposited and cycled Mn oxide (500 cycles). Mn oxide deposits were prepared at 20 mA cm^{-2} for 5 min at 75 rpm. **b** Mn 3s XPS peak splitting as a function of Mn oxidation state in Mn oxide. Data were compiled from Chigane et al. [30] (squares) and Gorlin and Jaramillo [31] (triangles)

respectively. Deposits of PEDOT only on Ni foam have a capacitance of 56 F g^{-1} , which indicates a synergistic effect between PEDOT and Mn oxide; the capacitance of the composite is more than the sum of its parts.

The mass loading of Mn oxide was around 3 mg cm^{-2} and that for the PEDOT coating was $0.5\text{--}1 \text{ mg cm}^{-2}$. At 5 mV s^{-1} , Ni foam samples exhibited areal capacitances of 500 and 290 mF cm^{-2} for deposits with and without PEDOT, respectively. Compared with the results from our previous work [19] on planar Au, the aerial capacitance has been significantly improved; deposits on Au with and without PEDOT had capacitances of 57 and 39 mF cm^{-2} , respectively. The Mn oxide deposits on Au had higher specific capacitances (285 and 195 F g^{-1} for coated and uncoated rods, respectively), but the flat substrate only sustained a mass loading of $0.15\text{--}0.2 \text{ mg cm}^{-2}$ before cracking, and delamination occurred.

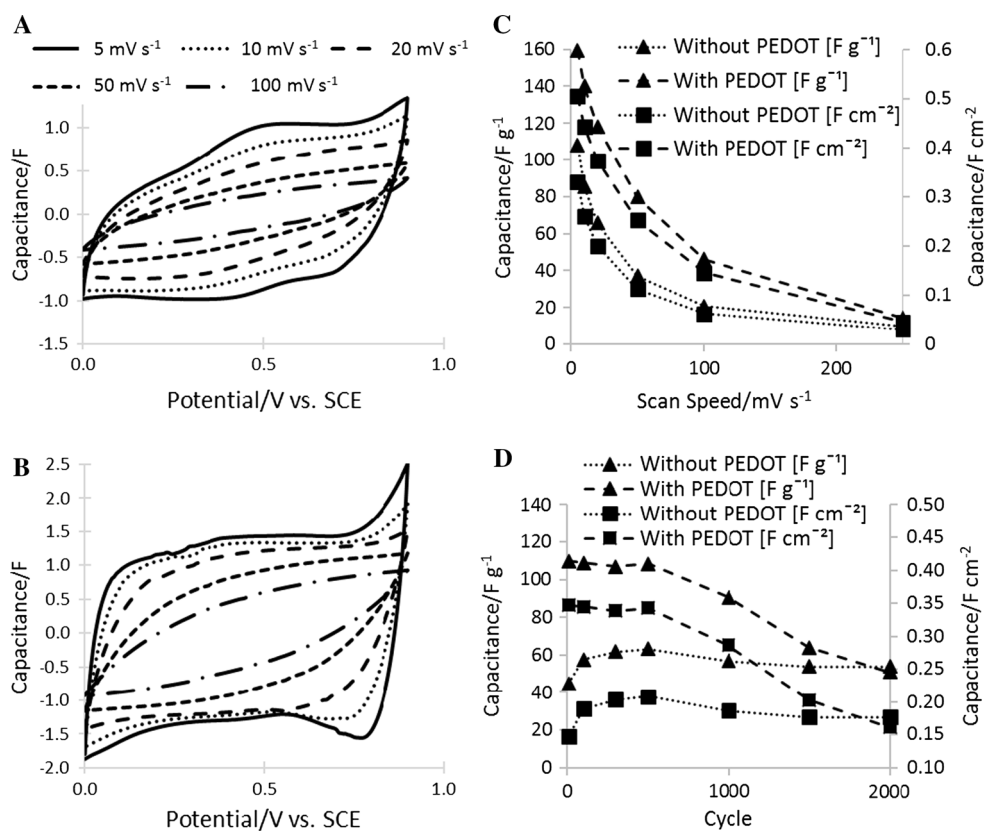
The capacitance values obtained on Ni foam are comparable with the lower-end values reported in the literature.

Yang et al. [28] reported a very high areal capacitance of 2.79 F cm^{-2} (67 F g^{-1}) for electrodeposited Mn oxide on Ni foam. Deposition was performed using cyclic voltammetry and resulted in a continuous flat layer across the surface of the Ni foam, extending over the porosity. The Ni foam acted as a conductive support, which allowed electrolyte access to both sides of the deposit. Yang et al. [28] obtained such a high areal capacitance because they were able to achieve a high mass loading without significantly compromising the specific capacitance. Although the specific capacitances of our deposits were higher than Yang et al.'s (159 for this work and 67 F g^{-1} for [28]), we were unable to increase the mass loading sufficiently to reach a very large areal capacitance. The mass loading of our deposits could be increased by using Ni foam with a smaller pore size or if deposition extended throughout the entirety of the foam, instead of just the first few layers.

Manganese oxide deposits without PEDOT exhibit good cyclability, as shown in Fig. 8d. Over the first 500 cycles, capacitance increased to 138 % of the initial capacitance. Over the next 500 cycles, the capacitance dropped slightly to 125 % of the original capacitance and stabilized at 120 % of the original capacitance between cycles 1000 and 2000. The capacitance increase is believed to be due to a combination of the change in oxidation state from Mn^{3+} to Mn^{4+} and dissolution and redeposition of material during cycling. MnO_2 has a higher specific capacitance than Mn_2O_3 . Manganese oxide deposits with PEDOT experienced very little capacitance change over the first 500 cycles. However, after 500 cycles, the capacitance began to drop, and at cycle 2000, the capacitance had dropped to 46 % of its initial value. The cyclability of deposits prepared on Ni foam vary somewhat compared with the results of our previous work on planar Au. PEDOT-coated Mn oxide rods had a capacitance retention of 92 % after 250 cycles, while uncoated Mn oxide rods had a retention of 75 %. [19] The difference in capacitance retentions for the flat Au and Ni foam substrates arises from the dissolution and redeposition of Mn oxide. Mn oxide that dissolves during the cathodic sweep can be redeposited during the anodic sweep. Redepleted material preferentially deposits in areas of good conduction, close to the substrate surface. For flat Au substrates, the entire surface is already covered with Mn oxide, leaving very little area for redeposition to occur. For Ni foam substrates, there is a significant amount of bare Ni exposed deep within the porosity to allow for redeposition. Ni foam facilitates redeposition of Mn oxide, leading to improved capacitance retention.

Figure 9 shows deposit morphologies after cycling. Figure 9a and e show deposits that have been cycled 500 times; Fig. 9a shows that the uncoated sample experiences significant fusing and delamination. Delamination breaks the electronic contact between the deposit and Ni current

Fig. 8 CV curves at varying scan speeds for deposits: **a** Without PEDOT and **b** with PEDOT. **c** Capacitance values at various scan speeds. **d** Capacitance values as a function of cycle number, at a scan rate of 20 mV s^{-1} . Mn oxide deposits were prepared at 20 mA cm^{-2} for 5 min at 75 rpm. The PEDOT coating was prepared at 1 V for 45 s



collector, causing a drop in capacitance. The fusion of the rods is caused by the redeposition of dissolved Mn oxide between rods in combination with volume changes during cycling. Up to cycle 500, the PEDOT coating successfully prevents the dissolution of the Mn oxide and subsequent fusion and delamination of the deposit. Aside from a small degree of cracking, deposits with PEDOT that have been cycled 500 times are nearly identical to uncycled deposits.

Figure 9b–d show uncoated deposits that have been cycled 2000 times. Note the structural differences within the cracks; for the uncoated sample, material has redeposited in areas of cracking. This redeposited material helps to maintain adhesion between the Mn oxide and Ni. For the PEDOT-coated sample, cracking of the Mn oxide/PEDOT deposit causes the film to curl and delaminate from the Ni (indicated by arrows in Fig. 9f). For the uncoated sample, significant dissolution and redeposition have occurred. The dissolved material redeposits in areas of good electronic conductivity, i.e., any exposed Ni. Redeposition of Mn oxide during cycling helps to reduce delamination of the deposit. If a section of the deposit begins to delaminate, material is deposited on the newly exposed Ni underneath the delaminated area, bridging the space between the Ni and the delaminated deposit with newly formed Mn oxide. The redeposited material has a very fibrous-high surface area morphology and is also in

areas of good conduction. These factors allow the redeposited material to have improved specific capacitance compared with the as-deposited Mn oxide rods, contributing to the capacitance improvement with cycling (along with the change in oxidation state from Mn^{3+} to Mn^{4+}). As the uncoated deposit is cycled, parts of the Mn oxide begin to peel, exposing the underlying Ni; Mn oxide is then able to redeposit onto the exposed Ni. The delamination and redeposition effects reach a dynamic equilibrium, causing the plateau in capacitance after cycle 1000. Figure 9c shows an area of successive cracking and redeposition of the uncoated deposit.

Images of a PEDOT-coated sample that has been cycled 2000 times are shown in Fig. 9f–h. Figure 9f shows that significant delamination of the deposit has occurred, indicated by arrows. During cycling, the PEDOT layer swells and shrinks, and after about 500 cycles, the PEDOT layer has degraded enough to allow for dissolution of the Mn oxide [4]. Unlike the uncoated sample, the Ni exposed during delamination experiences only a very small degree of Mn oxide redeposition; not enough material is redeposited to balance the capacitance loss from delamination. Figure 9g shows that only a few Mn oxide nuclei are present on the exposed Ni surface. Figure 9g and h also show that redeposition is concentrated between rods; the rods have fused together into a thick film. Mn oxide

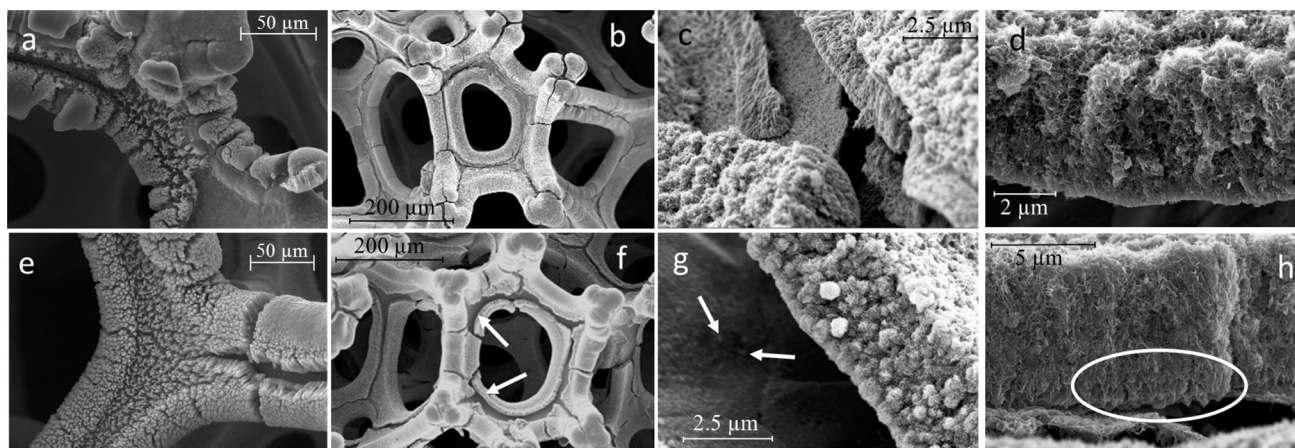


Fig. 9 SEM SE images of Mn oxide deposits after cycling. **a–d** Without PEDOT and **(e–h)** with PEDOT; **a, e** 500 cycles and **b–d, f–h** 2000 cycles. Areas of delamination are indicated with *arrows* in **f, c, g**. Higher magnification images of cracked regions of the deposits. Note the layers of redeposited Mn oxide in the uncoated sample and the minimal amounts of redeposited material (Ni grain boundaries are visible, and Mn oxide nuclei are indicated with *arrows*) in the

PEDOT-coated sample. **(d, h)** show cross-sectional views taken from cracks within the deposit. Note that for the uncoated sample, individual rods are apparent, whereas the coated rods experienced significant fusion of the rods; only the bases of the rods are visible (*circled*). Mn oxide deposits were prepared at 20 mA cm^{-2} for 5 min at 75 rpm. The PEDOT coating was prepared at 1 V for 45 s

redeposits more readily between rods than on the Ni, perhaps due to the enhanced conductivity provided by the PEDOT. Without the presence of the PEDOT coating, Mn oxide rods do not experience significant fusing, individual rods are still visible (Fig. 9d). The transition of the deposit from a rod-like structure to a thick film further enhances the delamination problem for PEDOT-coated deposits; volume changes during cycling lead to higher stresses for a fused deposit.

Although the capacitance (at 20 mV s^{-1} scan speed) for the PEDOT-coated sample at cycle 10 (110 F g^{-1} , 350 mF cm^{-2}) is significantly higher than that for the uncoated sample (45 F g^{-1} , 150 mF cm^{-2}), the capacitance loss experienced by the coated sample and the capacitance improvement of the uncoated sample resulted in similar capacitances after 2000 cycles (51 F g^{-1} , 160 mF cm^{-2} with PEDOT and 54 F g^{-1} and 180 mF cm^{-2} without PEDOT).

4 Conclusions

A template-free electrodeposition process has been developed to deposit high surface area Mn oxide and Mn oxide/PEDOT rods ($\sim 2 \mu\text{m}$ in diameter and several μm in length), for supercapacitor applications, onto porous Ni foam substrates. The Mn oxide deposits are poorly crystalline, with grain sizes of $\sim 5 \text{ nm}$, as determined through electron diffraction and imaging in the TEM. Cycled samples show improved crystallinity, and diffraction patterns can be indexed to a hexagonal birnessite MnO_2

crystal structure. Cycling changes the oxidation state for Mn oxide from Mn^{3+} to Mn^{4+} .

Capacitance was measured using cyclic voltammetry. The addition of PEDOT increased the maximum capacitance and improved the rate capability of the electrode. The maximum capacitances were 159 and 120 F g^{-1} (500 and 290 mF cm^{-2}) at 5 mV s^{-1} with and without PEDOT, respectively.

The cycling behaviors (at 20 mV s^{-1}) for uncoated and PEDOT-coated samples were different. For samples without PEDOT, there was an initial increase in capacitance during the first 500 cycles, followed by leveling off and a slight decrease; capacitance retention was 120 % after 2000 cycles. PEDOT-coated samples had higher initial capacitances, with little decrease over the first 500 cycles. This was followed by a steady capacitance decrease to 2000 cycles. The capacitance retention was 46 %; final capacitance values were comparable to those for uncoated Mn oxide after 2000 cycles. The capacitance increase during cycling for deposits without PEDOT can be explained by the change in oxidation state as well as dissolution and redeposition of Mn oxide, resulting in improved coverage of the Ni foam. Deposits with PEDOT experienced significant delamination during cycling (after 500 cycles), causing losses in electronic conductivity and capacitance.

Acknowledgments The authors acknowledge the financial support from the National Sciences and Engineering Research Council of Canada (NSREC). The authors would also like to thank Dr. Neda Dalili (NRC-NINT) and Dr. Anqiang He for their help with some of the electron microscopy work, Mr. Peng Li for HIM imaging, and Ms. Alisha Johnson for her help as a research assistant.

References

1. Simon P, Gogotsi Y (2008) Materials for electrochemical capacitors. *Nat Mater* 7:845–854
2. Ko R, Carlen M (2000) Principles and applications of electrochemical capacitors. *Electrochem Commun* 45:2483–2498
3. Wei W, Cui X, Chen W, Ivey DG (2011) Manganese oxide-based materials as electrochemical supercapacitor electrodes. *Chem Soc Rev* 40:1697–1721
4. Wang G, Zhang L, Zhang J (2012) A review of electrode materials for electrochemical supercapacitors. *Chem Soc Rev* 41:797–828
5. Wei W, Cui X, Mao X, Chen W, Ivey DG (2011) Morphology evolution in anodically electrodeposited manganese oxide nanostructures for electrochemical supercapacitor applications—effect of supersaturation ratio. *Electrochim Acta* 56:1619–1628
6. Liu C, Li F, Ma L-P, Cheng H-M (2010) Advanced materials for energy storage. *Adv Mater* 22:E28–E62
7. Toupin M, Brousse T, Be D (2004) Charge storage mechanism of MnO₂ electrode used in aqueous electrochemical capacitor. *Chem Mater* 16:3184–3190
8. Zheng JP, Cygan PJ, Jow TR (1995) Hydrous ruthenium oxide as an electrode material for electrochemical capacitors. *J Electrochem Soc* 142:2699–2703
9. Hu CC, Chen W-C, Chang K-H (2004) How to achieve maximum utilization of hydrous ruthenium oxide for supercapacitors. *J Electrochem Soc* 151:A281–A290
10. Zhang LL, Zhao XS (2009) Carbon-based materials as supercapacitor electrodes. *Chem Soc Rev* 38:2520–2531
11. Conway BE, Birss V, Wojtowicz J (1997) The role and utilization of pseudocapacitance for energy storage by supercapacitors. *J Power Sources* 66:1–14
12. Conway BE (1991) Transition from ‘supercapacitor’ to ‘battery’ behavior in electrochemical energy storage. *J Electrochem Soc* 138:1539–1548
13. Ghodbane O, Pascal JL, Favier F (2009) Microstructural effects on charge-storage properties in MnO₂-based electrochemical supercapacitors. *ACS Appl Mater Interfaces* 1:1130–1139
14. Stoller MD, Park S, Zhu Y, An J, Ruoff RS (2008) Graphene-based ultracapacitors. *Nano Lett* 8:3498–3502
15. Snook G, Kao P, Best AS (2011) Conducting-polymer-based supercapacitor devices and electrodes. *J Power Sources* 196:1–12
16. Bahloul A, Nessark B, Briot E, Groult H, Mauger A, Zaghbi K, Julien CM (2013) Polypyrrole-covered MnO₂ as electrode material for supercapacitor. *J Power Sources* 240:267–272
17. Huo Y, Zhang H, Jiang J, Yang Y (2012) A three-dimensional nanostructured PANI/MnOx porous microsphere and its capacitive performance. *J Mater Sci* 47:7026–7034
18. Babakhani B, Ivey DG (2010) Anodic deposition of manganese oxide electrodes with rod-like structures for application as electrochemical capacitors. *J Power Sources* 195:2110–2117
19. Babakhani B, Ivey DG (2010) Improved capacitive behavior of electrochemically synthesized Mn oxide/PEDOT electrodes utilized as electrochemical capacitors. *Electrochim Acta* 55:4014–4024
20. Dalili N, Clark MP, Davari E, Ivey DG (2016) Microstructural characterization of the cycling behavior of electrodeposited manganese oxide supercapacitors using 3D electron tomography. *J Power Sources* 328:318–328
21. Babakhani B, Ivey DG (2011) Effect of electrodeposition conditions on the electrochemical capacitive behavior of synthesized manganese oxide electrodes. *J Power Sources* 196:10762–10774
22. Hou Y, Cheng Y, Hobson T, Liu J (2010) Design and synthesis of hierarchical MnO₂ nanospheres/carbon nanotubes/conducting polymer ternary composite for high performance electrochemical electrodes. *Nano Lett* 10:2727–2733
23. Yu M, Zhai T, Lu X, Chen X, Xie S, Li W, Liang C, Zhao W, Zhang L, Tong Y (2013) Manganese dioxide nanorod arrays on carbon fabric for flexible solid-state supercapacitors. *J Power Sources* 239:64–71
24. Devaraj S, Munichandraiah N (2005) High capacitance of electrodeposited MnO₂ by the effect of a surface-active agent. *Electrochem Solid-State Lett* 8:A373–A377
25. Sun Z, Firdoz S, Yap EY-X, Li L, Lu X (2013) Hierarchically structured MnO₂ nanowires supported on hollow Ni dendrites for high-performance supercapacitors. *Nanoscale* 5:4379–4387
26. Xiao J, Yang S, Wan L, Xiao F, Wang S (2013) Electrodeposition of manganese oxide nanosheets on a continuous three-dimensional nickel porous scaffold for high performance electrochemical capacitors. *J Power Sources* 245:1027–1034
27. Xu P, Ye K, Cao D, Huang J, Liu T, Cheng K, Yin J, Wang G (2014) Facile synthesis of cobalt manganese oxides nanowires on nickel foam with superior electrochemical performance. *J Power Sources* 268:204–211
28. Yang J, Lian L, Ruan H, Xie F, Wei M (2014) Nanostructured porous MnO₂ on Ni foam substrate with a high mass loading via a CV electrodeposition route for supercapacitor application. *Electrochim Acta* 136:189–194
29. Jade XRD Software, Serial No. MDI-R99100, diffraction data retrieved from ICDD database, PDF# 18-0802, 13-0162
30. Chigane M, Ishikawa M, Izaki M (2001) Preparation of manganese oxide thin films by electrolysis/chemical deposition and electrochromism. *J Electrochem Soc* 148:D96–D101
31. Gorlin Y, Jaramillo TF (2010) A bifunctional nonprecious metal catalyst for oxygen reduction and water oxidation. *J Am Chem Soc* 132:13612–13614
32. Pei Q, Zuccarello G, Ahlskog M, Inganäs O (1994) Electrochromic and highly stable poly(3,4-ethylenedioxythiophene) switches between opaque blue-black and transparent sky blue. *Polymer* 35:1347–1351
33. Deguzman RN, Awaluddin A, Shen YF, Tian ZR, Suib SL, Ching S, Oyoung CL (1995) Electrical-resistivity measurements on manganese oxides with layer and tunnel structures—birnessites, todorokites, and cryptomelanes. *Chem Mater* 7:1286–1292